Supporting Information

Donor-acceptor-typed *β*-ketoenamine-linked covalent organic frameworks for enhanced photocatalytic hydrogen peroxide production

Yexuan Zhang,[a] Ning Liu,[a] Xiaoju Liu,[a] Qing Su,[b] Yanhui Zhao,[a] Liying Han,[a] Linfeng Gan,[c] Qiaolin Wu*[b] and Yang Lin*[a,d]

[a] *The Second Hospital of Jilin University, Jilin University, Changchun 130041, China. E-mail: zhangyexuancc@163.com*

[b] *College of Chemistry, Jilin University, Changchun, 130012, China.*

[c] *State Key Laboratory of Polymer Physics and Chemistry, Changchun Institute of Applied Chemistry, Chinese Academy of Sciences, Changchun 130022, PR China.*

[d] *Women's Hospital School of Medicine Zhejiang University Jilin Hospital, Changchun 130022, China.*

* *Corresponding authors.*

E-mail addresses: wuql@jlu.edu.cn (Qiaolin Wu), linyang1155@163.com (Yang Lin)

Section I. Materials and Methods

1. Materials

All reagents and solvents were used as received without further purification. 2,5-Diaminobenzonitrile was purchased from Adamas-Beta Shanghai Chemical Reagent Co., Ltd. (Shanghai, China). 2-Hydroxy-1,3,5-benzenetricarboxaldehyde and 1,3,5-triformylphloroglucinol were purchased from Haohong Biomedical Technology Co., Ltd. (Shanghai, China). Mesitylene, 1,4-dioxane, and silver nitrate ($AgNO_3$) were purchased from Energy Chemical Company (Shanghai, China). Tetrahydrofuran (THF), methanol, *N*,*N*-dimethylformamide (DMF), and ethanol (EtOH) were purchased from Tianjin Tiantai Chemicals Co., Ltd. (Tianjin, China).

2. General Characterizations

Powder X-ray diffraction (PXRD) patterns were recorded using a PANalytical B.V. Empyrean diffractometer, with samples deposited as powders on glass plates at room temperature. Fourier-transform infrared (FTIR) spectra were acquired on a Thermo Scientific Nicolet iS5 spectrometer using KBr compression testing. COF structures were visualized via Materials Studio software. X-ray photoelectron spectroscopy (XPS) analyses were performed on a Thermo ESCALAB 250 spectrometer. Solid-state ^{13}C cross-polarization magic angle spinning nuclear magnetic Resonance (^{13}C CP-MAS NMR) spectra were recorded using a Bruker DRX spectrometer. Thermogravimetric analysis (TGA) was conducted on a NETZSCH STA499F3 simultaneous thermal analyzer, with measurements carried out under nitrogen atmosphere from room temperature to 800 °C at a heating rate of 10 °C min^{-1}. Nitrogen adsorption-desorption isotherms were measured at 77 K using a Quantachrome instrument; prior to analysis, samples were vacuum-dried at 80 °C for over 4 h. The Brunauer-Emmett-Teller (BET) method was used to calculate specific surface areas, and pore size distribution curves were derived from BJH desorption data. Water contact angles were measured on a Kruss DSA 100 goniometer using 3 μL water droplets. Scanning electron microscopy (SEM) images were obtained with a Hitachi SU8000 microscope, and transmission electron microscopy (TEM) analyses were performed using a Philips-FEI Tecnai G2 F20 S-TWIN microscope. Ultraviolet-visible diffuse reflectance spectra (UV-vis DRS) were recorded on a Shimadzu UV-2700 spectrophotometer. Steady-state photoluminescence (PL) and time-resolved PL lifetime measurements were conducted using an FLS920 spectrophotometer. Electron paramagnetic resonance (EPR) spectra were acquired with a Bruker tyFA200 ESR spectrometer. Photoelectrochemical and electrochemical measurements

were performed on a CHI760E electrochemical workstation (Shanghai Chenhua Instrument Co., Ltd.) using a standard three-electrode system, where an Ag/AgCl electrode served as the reference and a Pt electrode as the counter electrode.

3. Theoretical calculations

All calculations were performed using Gaussian 16[1]. The selected structures of COFs containing ORR active sites were chosen as fragments for analysis. The M06-2X functional with the 6-31G(d,p) basis set was employed, with the D3 dispersion correction included to account for dispersion interactions. The PCM implicit solvent model was used to investigate the effect of solvent polarity in water. Geometry optimizations and frequency calculations were carried out for each configuration. The Multiwfn 3.8 (dev) program[2] was used to analyze the HOMO, LUMO energy levels, and electrostatic potential,[2,3] while VMD software was utilized for the visualization of frontier orbitals and electrostatic potentials.[4] Based on the frequency calculations, single-point energy calculations were performed using M06-2X/6-311G(d,p). Thermodynamic quantities at 298.15 K in the solvent environment were calculated using the quasi-RRHO model via the Shermo program,[5] to determine the thermodynamic energy changes associated with oxygen adsorption and the Gibbs free energy changes during the ORR process for each COF. The adsorption energy is given by $E_{ads} = E_{ab} - E_a - E_b$ (E_{ab} represents the total energy of the COF fragment after adsorbing oxygen, E_a is the energy of the COF fragment, and E_b is the energy of the oxygen molecule). The free energy (*G)* of a gas-phase molecule or an adsorbate on the surface was calculated using the equation ($G = E + ZPE - TS$), where (E) is the total energy, (ZPE) is the zero-point energy, (T) is the temperature in Kelvin (298.15 K is used here), and (S) is the entropy.

4. Methods

Synthesis of COF-TpDb

According to prior reports,[6–8] COF-TpDb was synthesized via a modified solvothermal Schiff Base condensation as follows: 1,3,5-triformylphloroglucinol (21 mg, 0.1 mmol), 2,5-diaminobenzonitrile (19.9 mg, 0.15 mmol), mesitylene (1 mL), 1,4-dioxane (1 mL) and acetic acid (6 M, 0.2 mL) were filled into a Pyrex tube. The mixture was sonicated for 10 minutes, frozen at 77 K (liquid N_2 bath) and degassed via three freeze-pump-thaw cycles. The vessel was then flame sealed and heated at 120 °C for 3 days. The product was collected by centrifugation (10 minutes) and washed three times with DMF, THF and acetone to eliminate residual guests, followed by

Soxhlet extraction with THF for 24 h. Finally, the dark red powder was dried under vacuum at 80 °C overnight, yielding COF-TpDb (33.7 mg, 95%).

Synthesis of COF-HbDb

To synthesize COF-HbDb, 2-hydroxy-1,3,5-benzenetricarboxaldehyde (17.8 mg, 0.1 mmol), 2,5-diaminobenzonitrile (19.9 mg, 0.15 mmol), mesitylene (1.2 mL), 1,4-dioxane (0.8 mL), and 6 M acetic acid (0.2 mL) were loaded into a Pyrex tube. The reaction mixture then underwent sonication for 10 min, freezing at 77 K (liquid N_2 bath), and three freeze-pump-thaw degassing cycles. Subsequently, the vessel was flame sealed. After heating at 120 °C for 3 days, a solid product was obtained and isolated by centrifugation (10 minutes). The solid was washed thrice with DMF, THF and acetone to remove residual species, followed by 24 h Soxhlet extraction with THF. Vacuum drying at 80 °C overnight yielded dark red COF-HbDb (26.2 mg, 81%).

Photocatalytic H_2O_2 production

5 mg catalysts and 50 mL deionized water were placed in a hermetically sealed reactor consisting of a quartz tube. The suspension was ultrasonically dispersed for 15 min, followed by bubbling O_2 into the suspension for 30 min in the dark. Prior to photocatalytic tests, the suspension was stirred for 30 min in the dark to achieve adsorption-desorption equilibrium. A 300 W Xe lamp (CEL-HXF300-T3 CEAULIGHT) was used as the light source, with O_2 continuously bubbled into the reactor. A cutoff filter and optical path converter were used to generate simulated sunlight (AM 1.5G, 300−1100 nm), The light intensity was maintained at 100 mW cm^{-2}, which was measured and calibrated using a five-point method with a fully automated optical power meter (CEL-NP2000-2A, CEAULIGHT).

To evaluate the effect of gas atmosphere (O_2, Air and N_2), N_2 was purged into the reaction system for 30 min in the dark to remove residual O_2, followed by photocatalysis under continuous N_2 flow. In order to explore the influence of different sacrificial agents and investigate the reaction process of photocatalytic H_2O_2 production, Nitrotetrazolium Blue Chloride (NBT, 4 mg, for $O_2^{\bullet-}$ detection), *tert*-butanol (TBA, 9.4 μL, for •OH scavenging), $AgNO_3$ (17 mg, 0.1 mmol) and sacrificial agents (10 vol%) were added to the reaction system respectively, under identical conditions.

Determination of H_2O_2 concentration (Cerium sulfate method)

1 mL of the catalytic reaction suspension was filtered through a 0.22 μm membrane to remove

catalyst particles, then mixed with a pre-prepared $Ce(SO_4)_2$ solution (prepared by dissolving 83.1 mg $Ce(SO_4)_2$ in 250 mL of 0.5 M H_2SO_4) for absorbance measurement. The yellow Ce^{4+} solution can be reduced by H_2O_2 to colorless Ce^{3+} (Eq. S1). The concentrations of Ce^{4+} before and after the reaction were measured using a UV-vis spectrophotometer at a detection wavelength of 318 nm. A linear relationship exists between the Ce^{4+} concentration and its UV absorption intensity, with the absorption spectrum and standard curve provided in Fig. S1. Then the H_2O_2 concentration was determined by calculating the amount of Ce^{4+} reacted with H_2O_2 (Eq. S2).

$2Ce^{4+} + H_2O_2 \rightarrow 2Ce^{3+} + 2H^+ + O_2$ (Eq. S1)

The concentration of H_2O_2 was calculated using the equation:

$c(H_2O_2) = 1/2 \times \Delta c(Ce^{4+})$ (Eq. S2)

The AQY measurement

The apparent quantum yields (AQY) of the two COFs were measured at λ = 420, 450, 500, 550, 600 and 650 nm using single-wavelength filters. The photocatalytic reaction was conducted in a photocatalytic reactor with 20 mL deionized water and 16 mg catalyst. After sonication dispersion for 15 minutes, and bubbling for 30 minutes under dark conditions, the bottle was irradiated by an Xe lamp (AM 1.5G, 300−1100 nm, CEL-HXF300-T3 CEAULIGHT, Beijing China Education Au-light Technology Co., LTD., Beijing, China). The irradiation area was 4.91 cm^2. AQY is calculated from the following equation:

$$AQY\% = \frac{[H_2O_2 production\ (mol)] \times 2}{Photon\ number\ entered\ into\ the\ reactor\ (mol)} \times 100$$
$$= \frac{[N_a \times h \times c][H_2O_2 production\ (mol)] \times 2}{I \times S \times t \times \lambda} \times 100$$

Where N_a was the Avogadro constant (6.022×10^{23} mol^{-1}), h is the Planck constant (6.626×10^{-34} J·s), c is the speed of light (3×10^8 m s^{-1}), I is the intensity of irradiation light (W cm^{-2}), S is the irradiation area (cm^2), t is the irradiation time (s), λ is the wavelength of the monochromatic

light (m).

Section II. Supplementary figures and tables

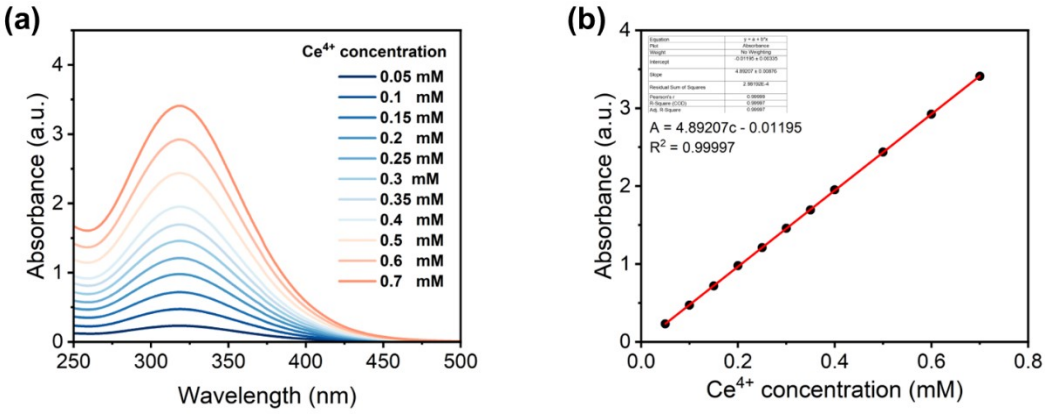

Fig. S1 (a) UV-visible absorption curves of $Ce(SO_4)_2$ solutions of different concentrations. (b) Fitting curve of $Ce(SO_4)_2$ concentrations versus absorption intensities.

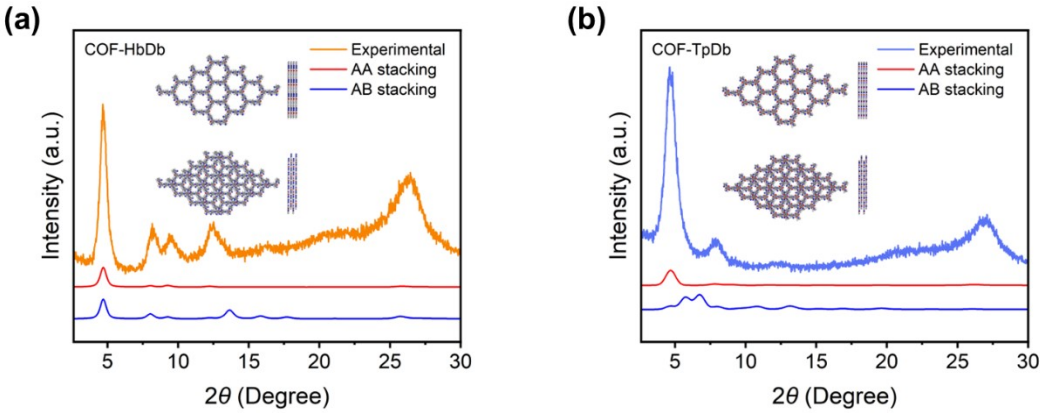

Fig. S2 PXRD patterns for different stacking modes (AA and AB) of COF-HbDb (a) and COF-TpDb (b).

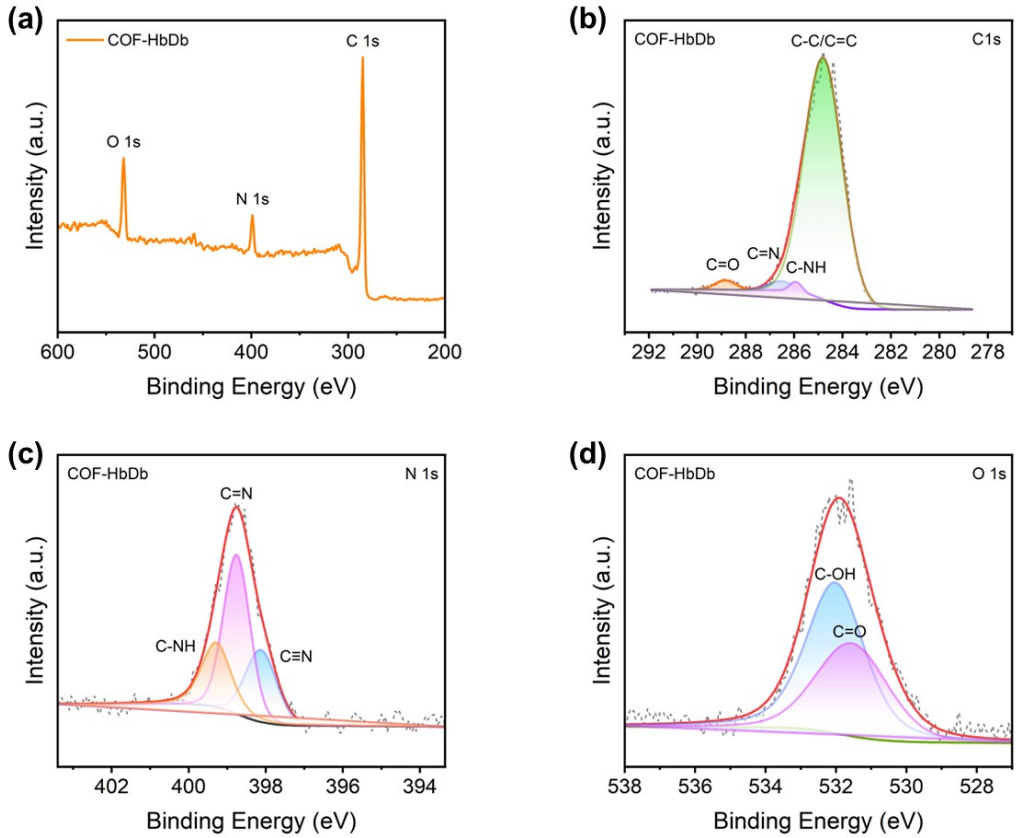

Fig. S3 X-ray photoelectron spectra of COF-HbDb. (a) Survey spectrum; (b) High-resolution C 1s spectrum; (c) High-resolution N 1s spectrum; (d) High-resolution O 1s spectrum.

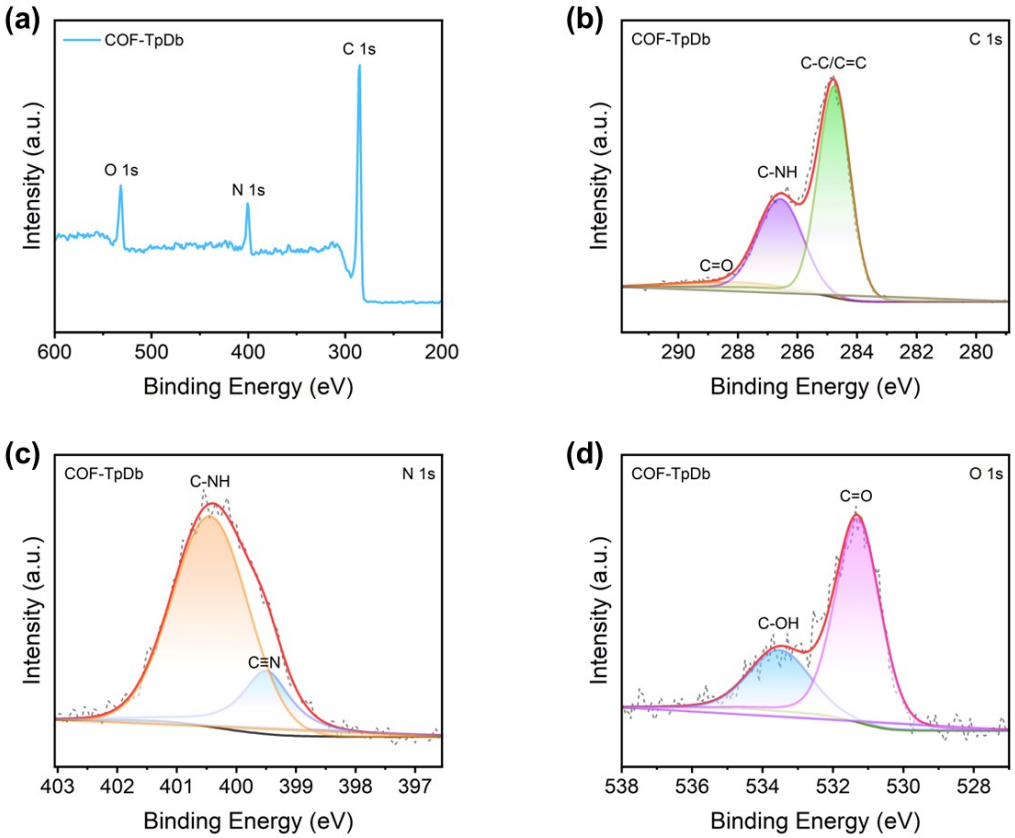

Fig. S4 X-ray photoelectron spectra of COF-HbDb. (a) Survey spectrum; (b) High-resolution C 1s spectrum; (c) High-resolution N 1s spectrum; (d) High-resolution O 1s spectrum.

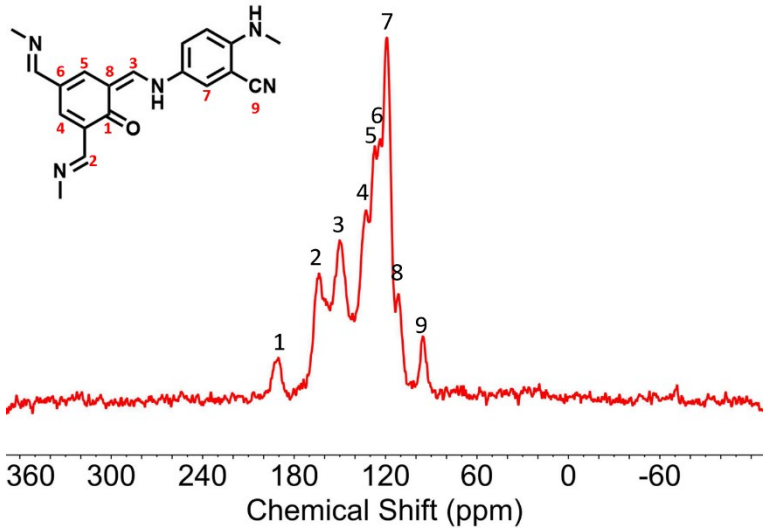

Fig. S5 Solid-state ^{13}C cross-polarization magic angle spinning NMR spectrum of COF-HbDb.

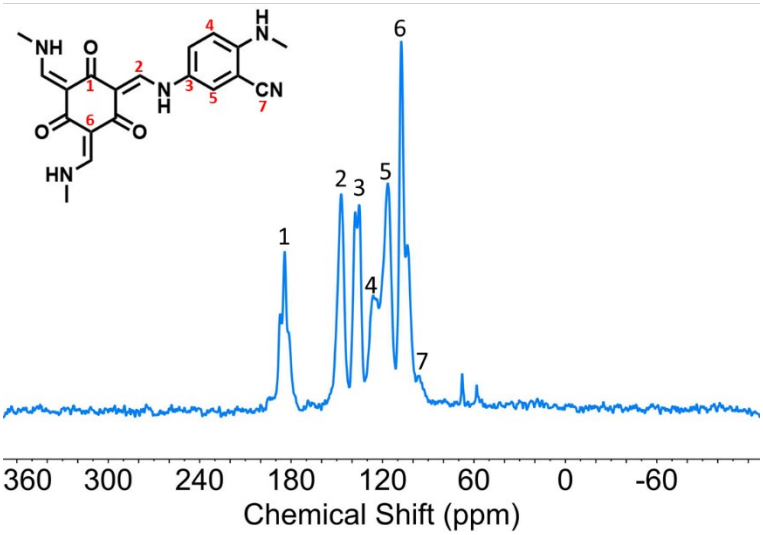

Fig. S6 Solid-state ^{13}C cross-polarization magic angle spinning NMR spectrum of COF-TpDb.

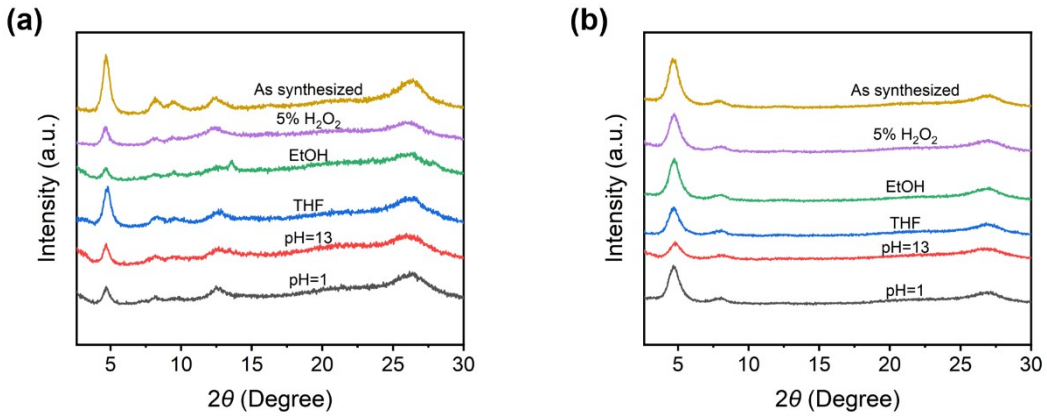

Fig. S7 PXRD patterns of COF-HbDb (a) and COF-TpDb (b) before and after treatment under diverse conditions.

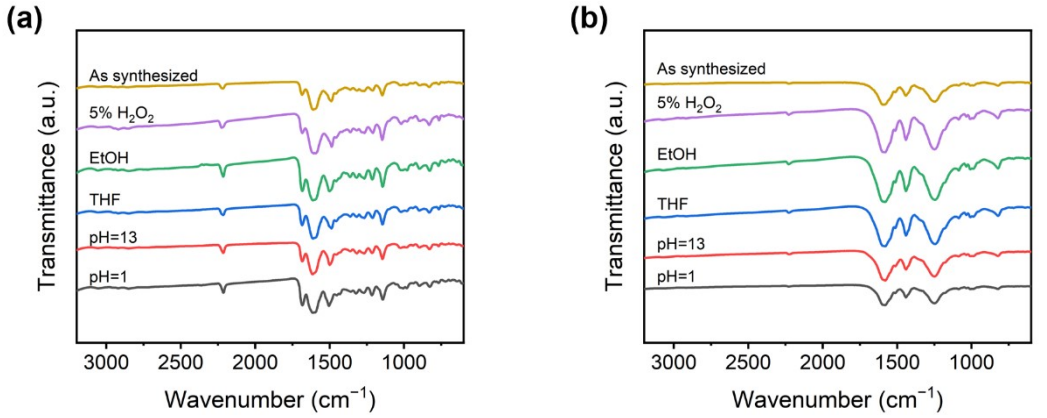

Fig. S8 FTIR spectra of COF-HbDb (a) and COF-TpDb (b) before and after treatment under

diverse conditions.

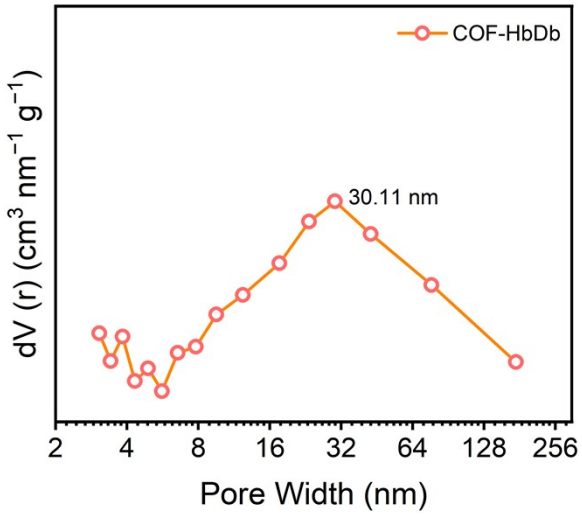

Fig. S9 The pore size distributions of COF-HbDb.

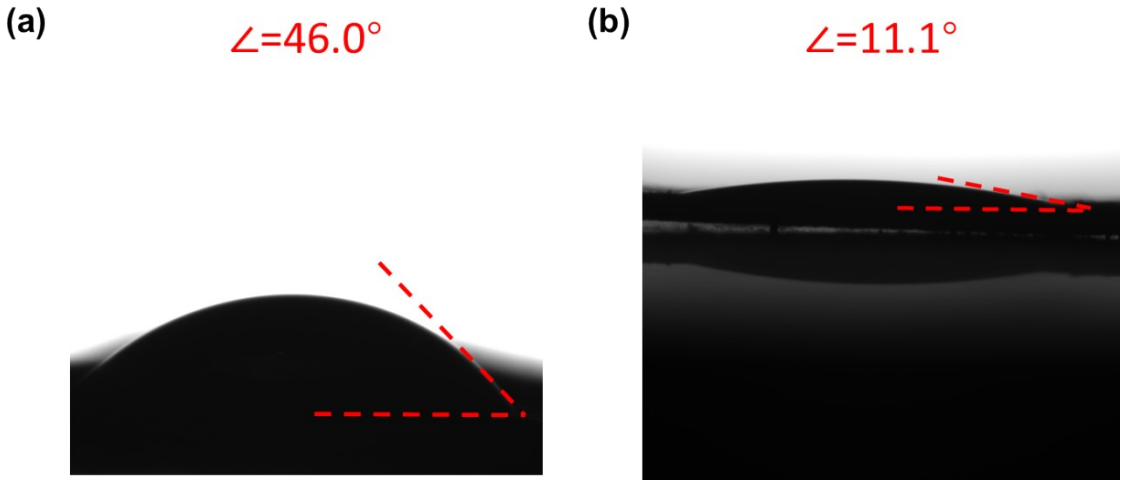

Fig. S10 The water contact angles of COF-HbDb (a) and COF-TpDb (b).

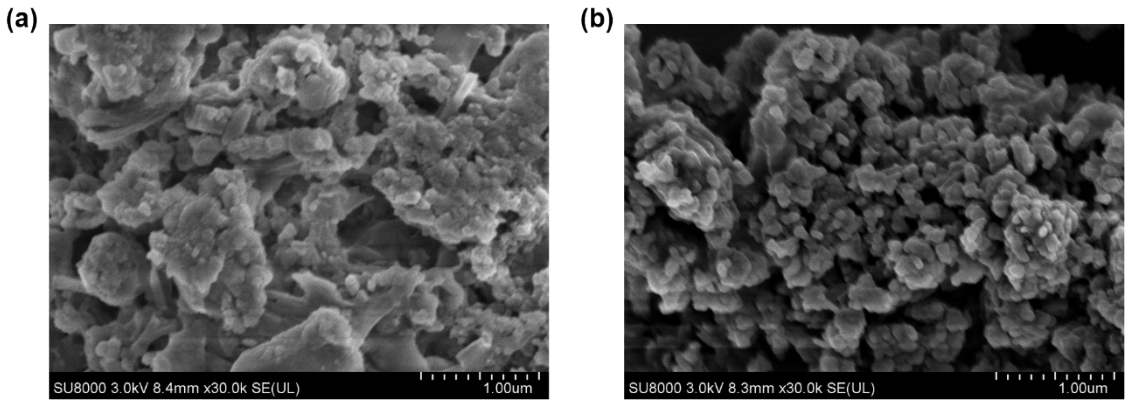

Fig. S11 The SEM images of COF-HbDb (a) and COF-TpDb (b).

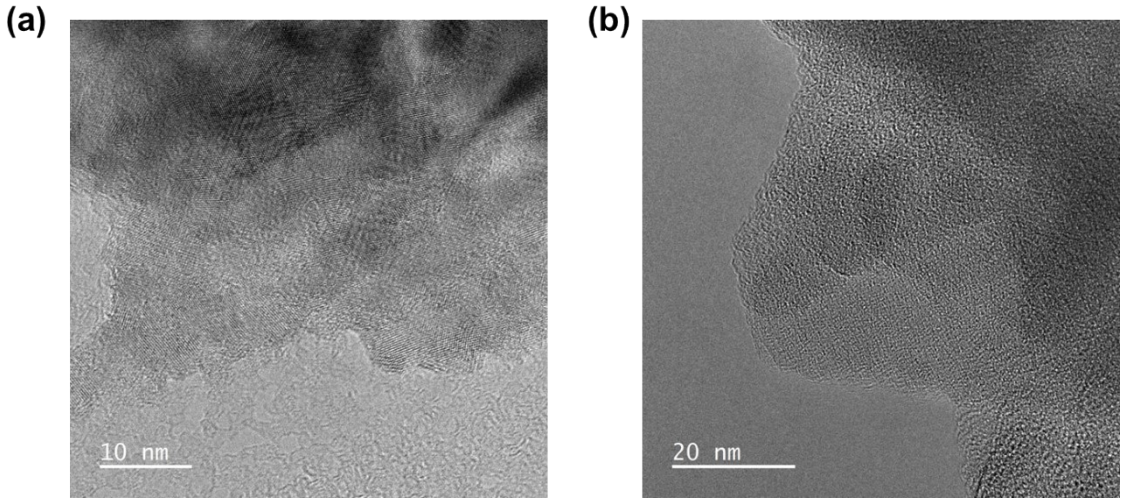

Fig. S12 The HR-TEM images of COF-HbDb (a) and COF-TpDb (b).

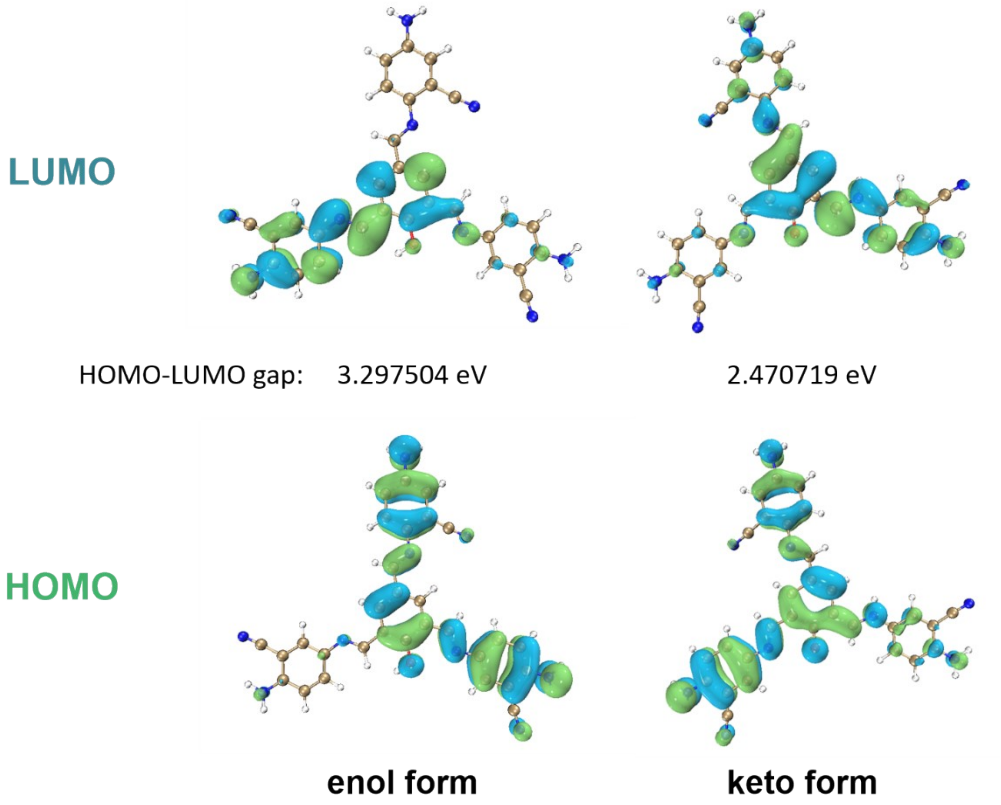

Fig. S13 Calculated charge distributions and energy gaps of the HOMO/LUMO for COF-HbDb.

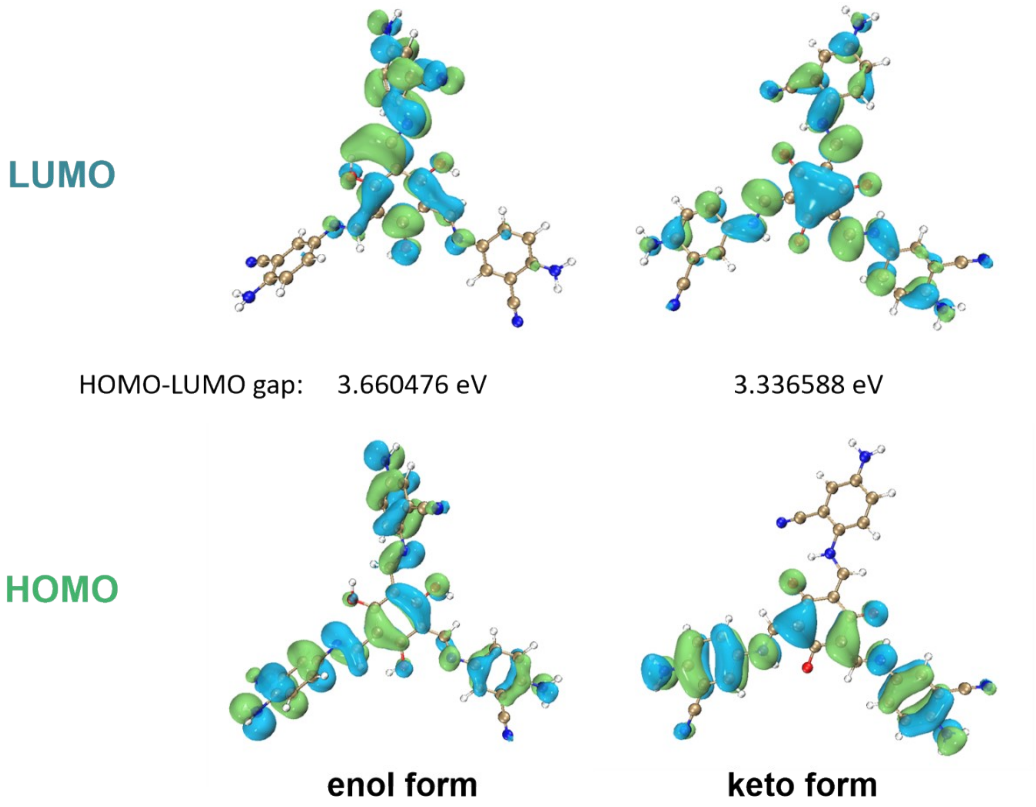

Fig. S14 Calculated charge distributions and energy gaps of the HOMO/LUMO for COF-TpDb.

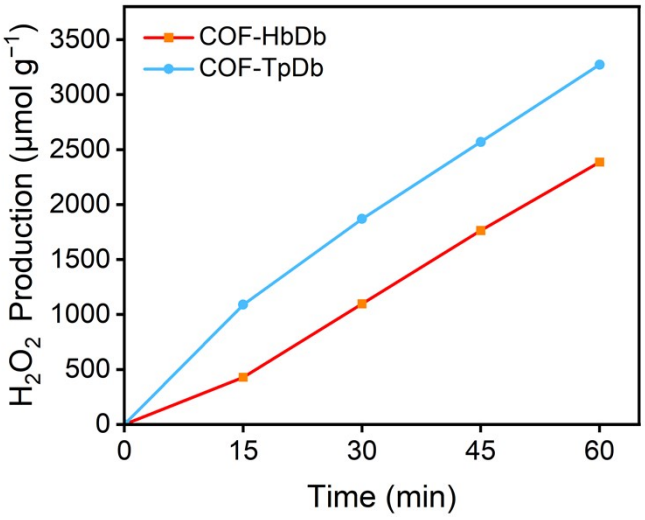

Fig. S15 Photocatalytic production of H_2O_2 over COF-HbDb and COF-TpDb with time dependence.

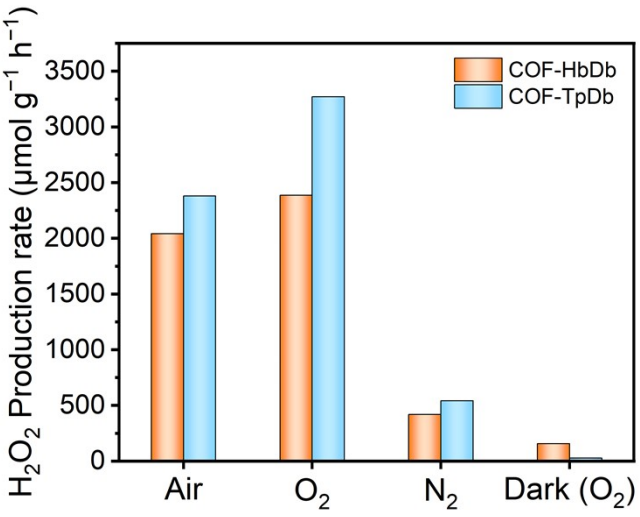

Fig. S16 Photocatalytic production of H_2O_2 under different atmosphere over COF-HbDb and COF-TpDb.

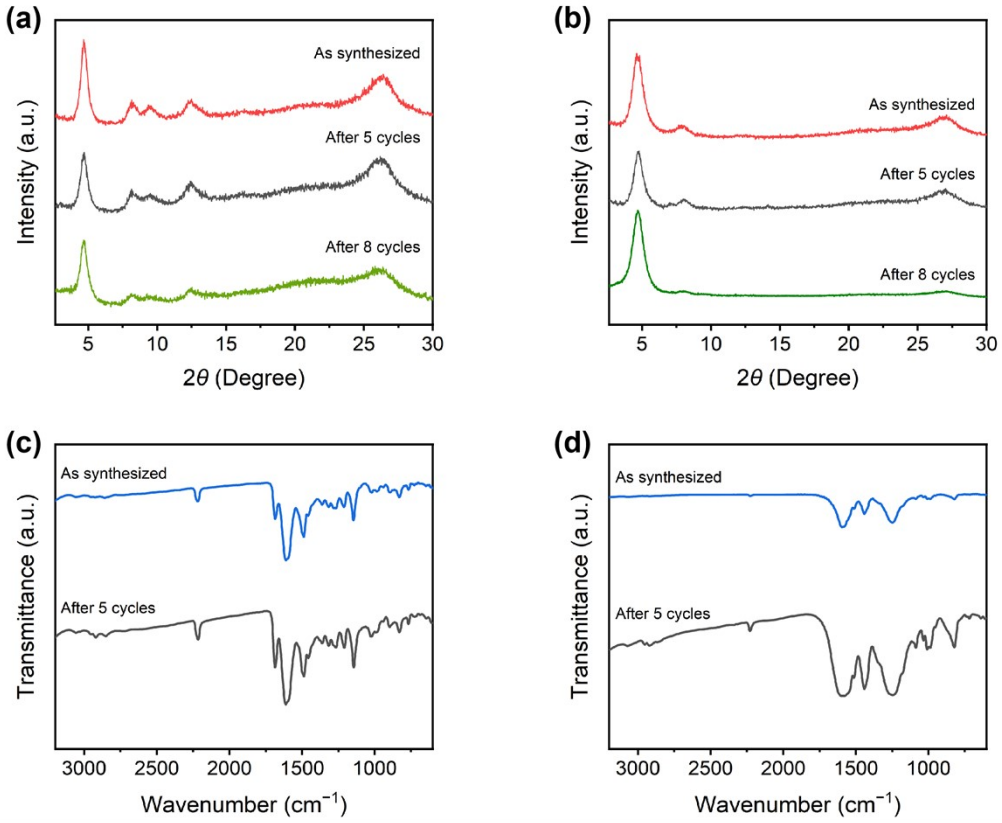

Fig. S17 PXRD patterns and FTIR spectra of COF-HbDb (a, c) and COF-TpDb (b, d) before and after cycle reactions.

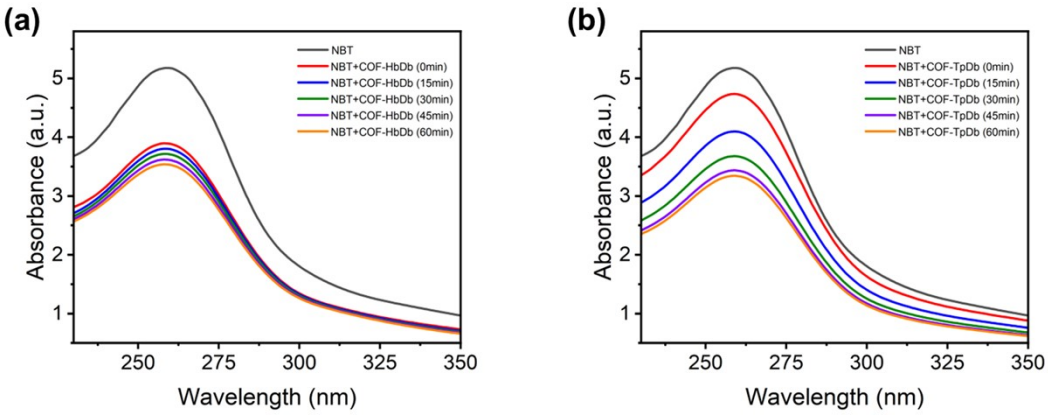

Fig. S18 The photocatalytic production of $O_2^{\bullet-}$ on COF-HbDb (a) and COF-TpDb (b) detected by NBT method.

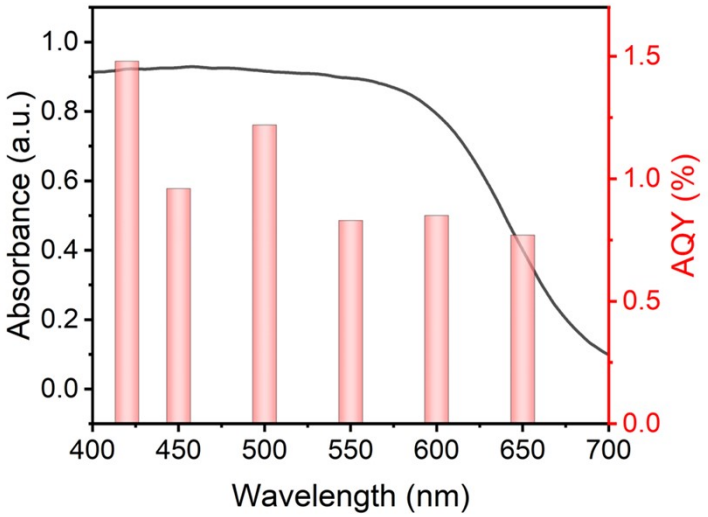

Fig. S19 AQY (bar chart) and UV–vis DRS curve (black line) of COF-HbDb.

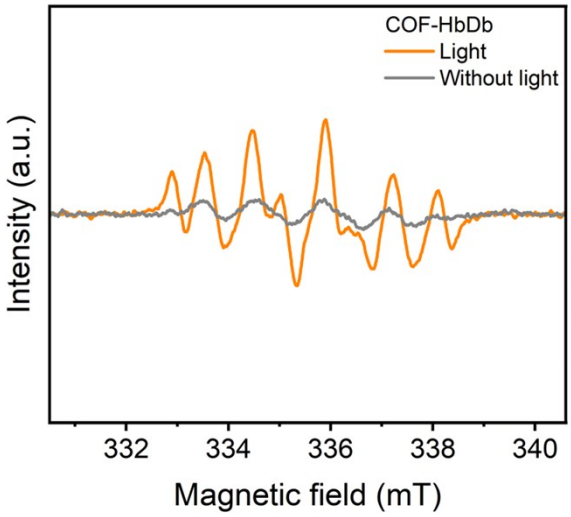

Fig. S20 EPR spectra of DMPO trapped $O_2^{\bullet-}$ of COF-HbDb.

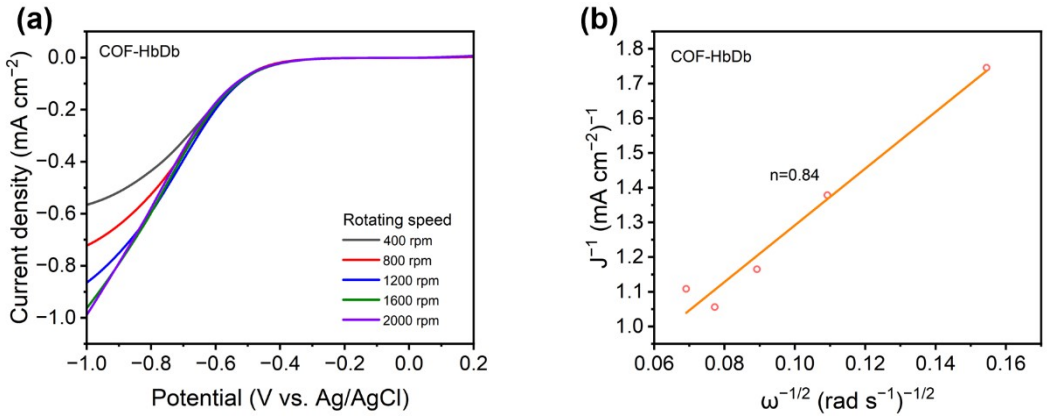

Fig. S21 Linear sweep voltammetry (LSV) curves at different rotating speeds and Kouteckly–Levich plots of COF-HbDb obtained from RDE measurement.

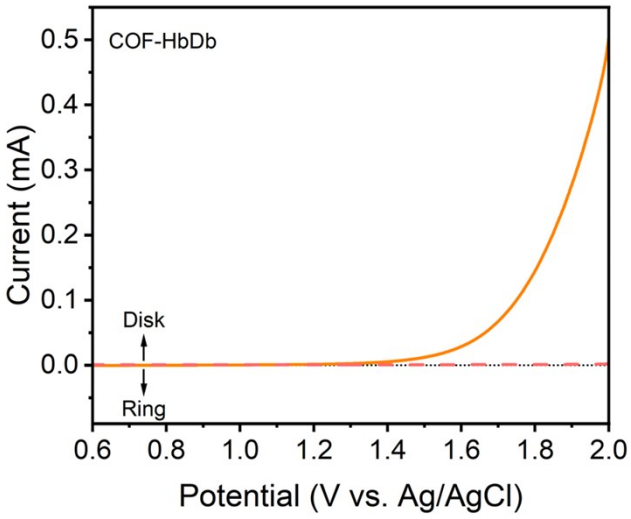

Fig. S22 RRDE measurement of COF-HbDb conducted in 0.1 M phosphate buffer solution (pH = 7) at 1000 rpm, with the Pt ring electrode potential set to 0.6 V vs. Ag/AgCl for H_2O_2 detection.

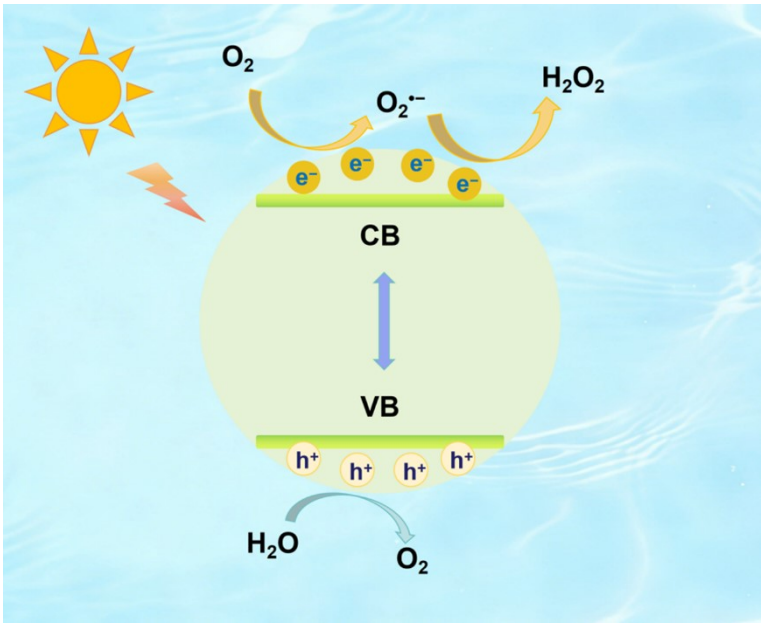

Fig. S23 Proposed mechanism of photocatalytic H_2O_2 production for COF-HbDb and COF-TpDb.

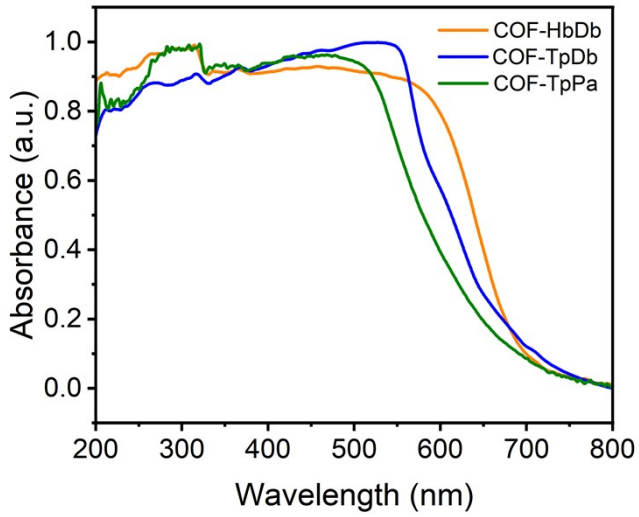

Fig. S24 Comparison of UV−vis DRS spectra of COF-HbDb, COF-TpDb, and COF-TpPa.

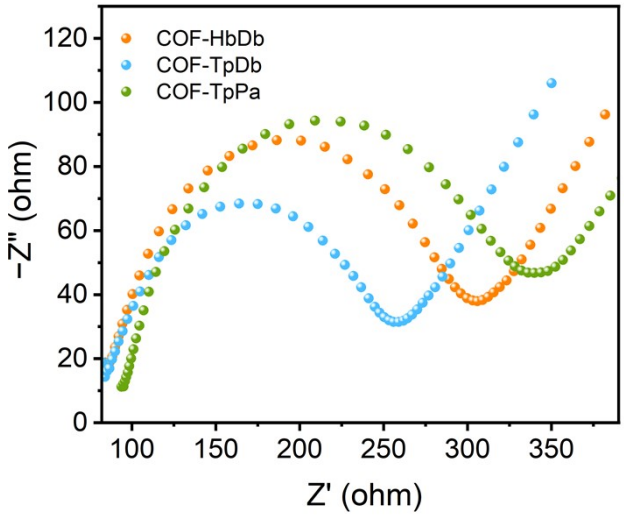

Fig. S25 Electrochemical impedance spectra of the three COFs.

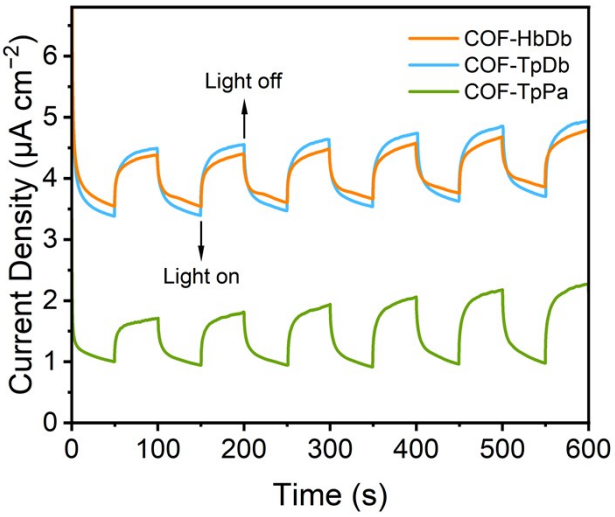

Fig. S26 Transient photocurrent density of the three COFs.

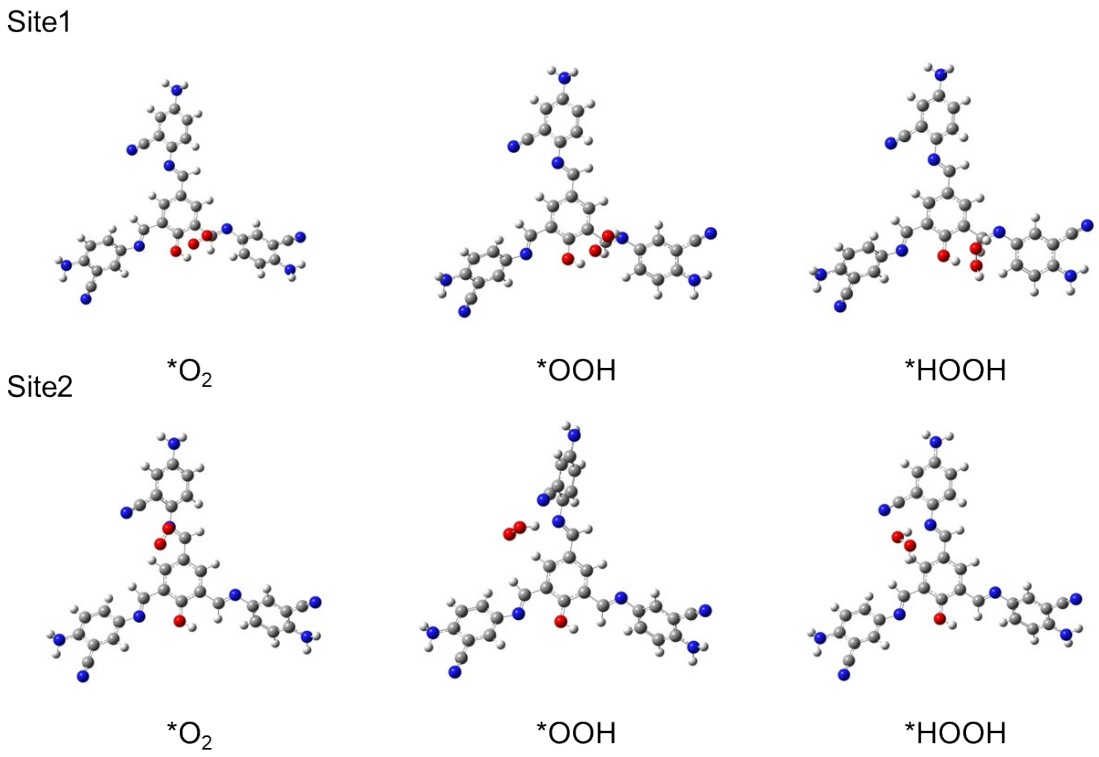

Fig. S27 Adsorption configuration of *O_2, *OOH and *HOOH intermediates on two possible active sites on COF-HbDb (enol form). DFT-calculated O_2 Eads (Site 1) = 6.279 kcal/mol, Eads (Site 2) = 6.142 kcal/mol.

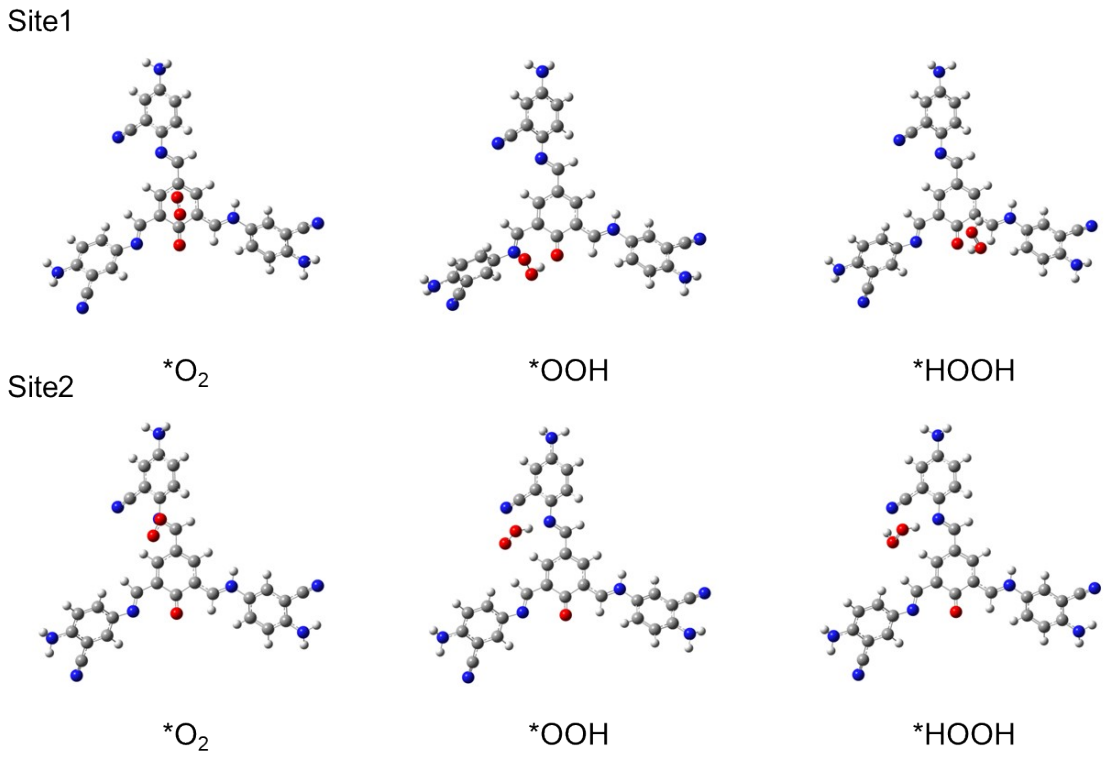

Fig. S28 Adsorption configuration of $*O_2$, *OOH and *HOOH intermediates on two possible active sites on COF-HbDb (keto form). DFT-calculated O_2 Eads (Site 1) = 5.399 kcal/mol, Eads (Site 2) = 5.477 kcal/mol.

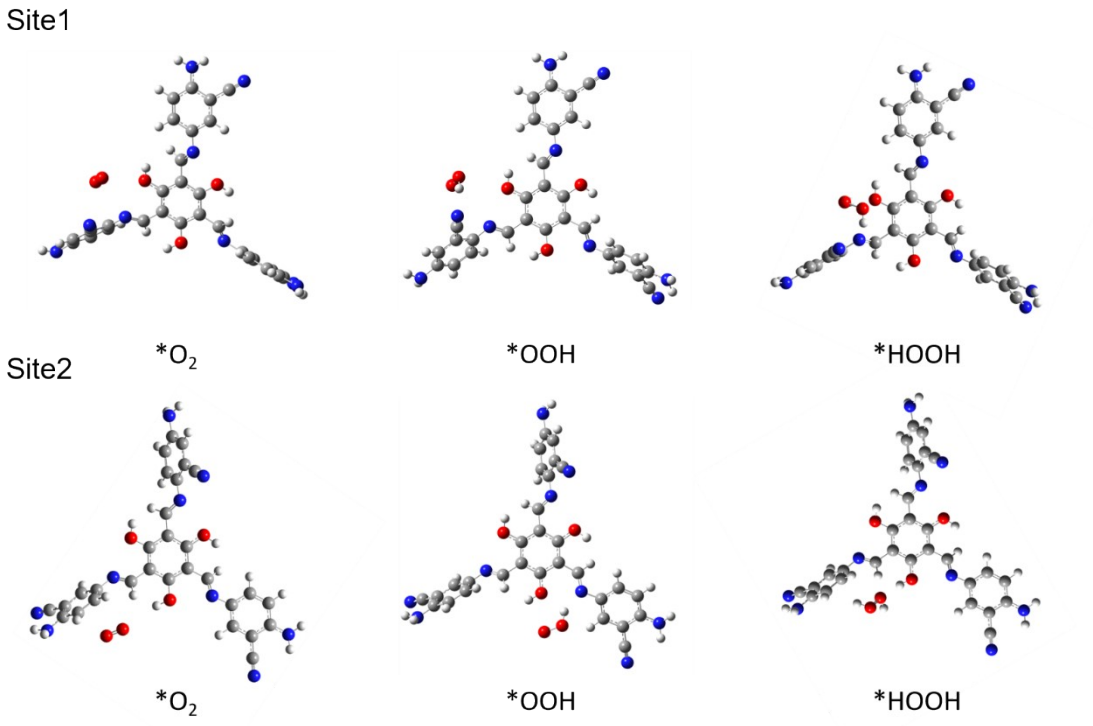

Fig. S29 Adsorption configuration of $*O_2$, *OOH and *HOOH intermediates on two possible active sites on COF-TpDb (enol form). DFT-calculated O_2 Eads (Site 1) = 1.374 kcal/mol, Eads (Site 2) = 0.933 kcal/mol.

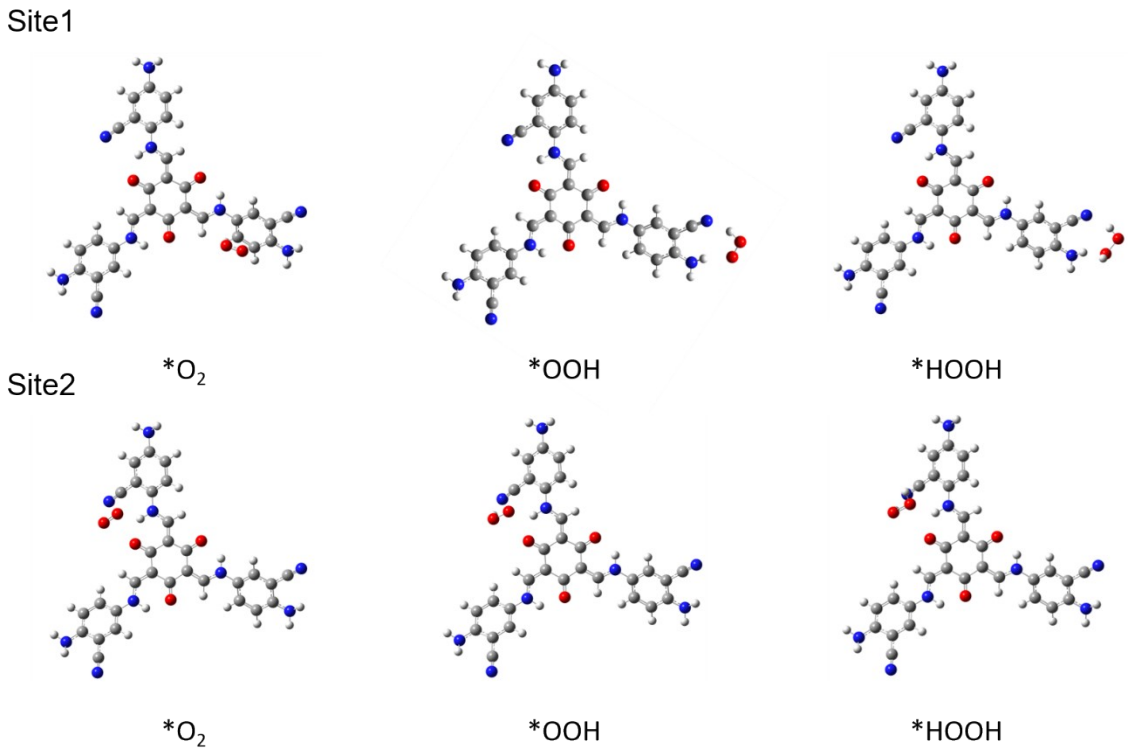

Fig. S30 Adsorption configuration of $*O_2$, *OOH and *HOOH intermediates on two possible active sites on COF-TpDb (keto form). DFT-calculated O_2 Eads (Site 1) = 1.586 kcal/mol, Eads (Site 2) = 1.506 kcal/mol.

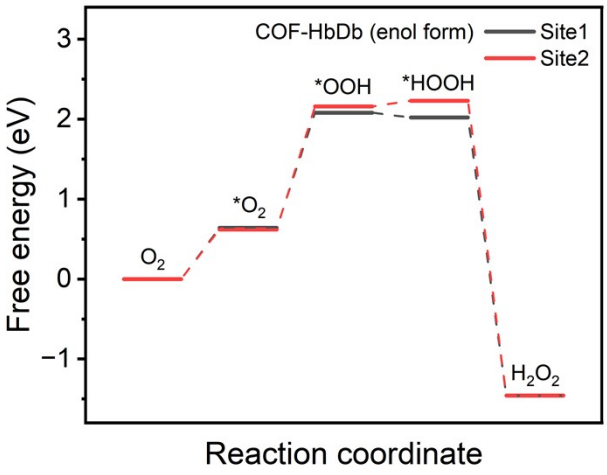

Fig. S31 Gibbs free energy diagrams of COF-HbDb (enol form) for H_2O_2 photogeneration by indirect $2e^-$ ORR pathway.

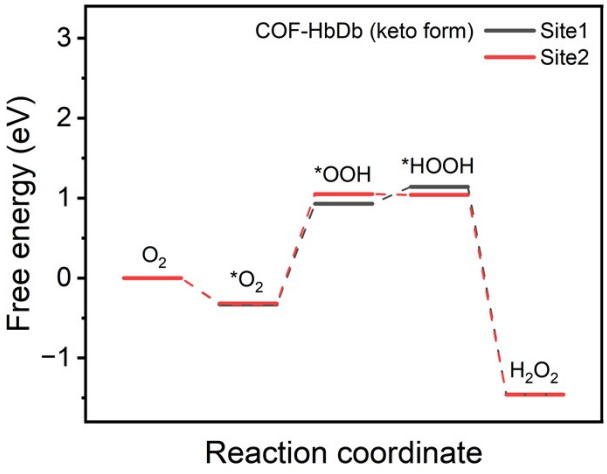

Fig. S32 Gibbs free energy diagrams of COF-HbDb (keto form) for H_2O_2 photogeneration by indirect $2e^-$ ORR pathway.

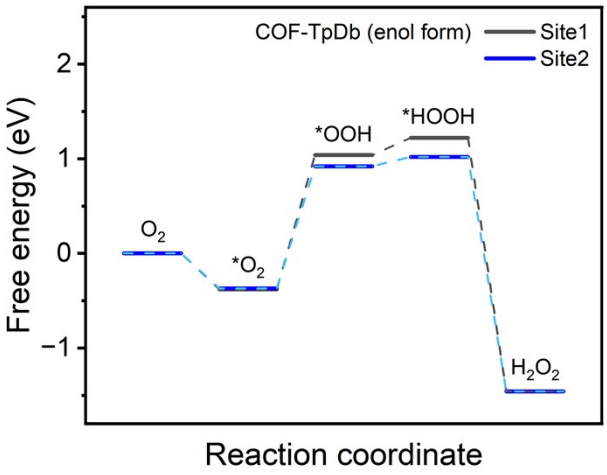

Fig. S33 Gibbs free energy diagrams of COF-TpDb (enol form) for H_2O_2 photogeneration by indirect $2e^-$ ORR pathway.

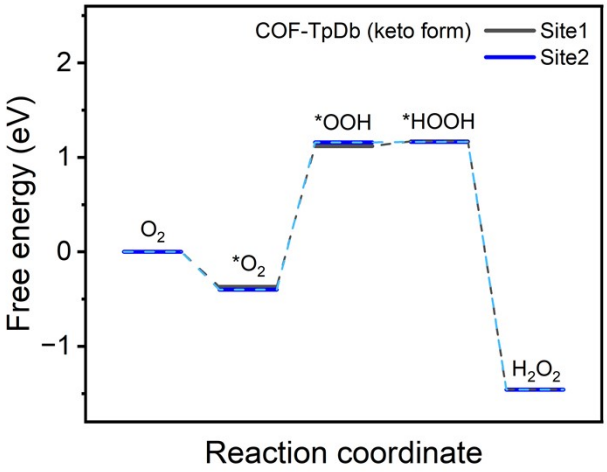

Fig. S34 Gibbs free energy diagrams of COF-HbDb (keto form) for H_2O_2 photogeneration by indirect $2e^-$ ORR pathway.

Tab. S1 Comparison of photocatalytic H_2O_2 production performance among recently reported COF−based photocatalysts.

Photocatalyst	**Conditions**	**Illumination**	**H_2O_2 production rate (μmol g^{-1} h^{-1})**	**Reference**
COF-TpDb	H_2O, O_2	AM 1.5G	3272	This work
COF-HbDb	H_2O, O_2	AM 1.5G	2386	This work
TpBD-COF-B	H_2O, Air	λ > 420 nm	533	*J. Environ. Sci.*, 2025, 153, 172–181
HITMS-COF-20	H_2O, O_2	λ > 420 nm	452	*ACS Catal.*, 2025, 15, 5683–5693
CQDs@COF-3.5	H_2O, O_2	λ > 420 nm	1380	*Catal. Today*, 2025, 459, 115399
BTD-sp^2c-COF	H_2O, Air	λ > 420 nm	1139	*ACS Appl. Mater. Interfaces*, 2025, 17, 1097–1109
Mo-DHTA COF	H_2O, Air	λ = 467 nm	383	*Small*, 2025, 21, 2501823
TAPT-2KtTb Pd COF	H_2O, O_2	λ > 420 nm	2676.3	*Small*, 2025, 21, 2409006
N_2-COF	H_2O, O_2	λ > 420 nm	3341	*Small*, 2025, 2500674–2500686
TOTP2.4	H_2O, Air	350 nm ≤ λ ≤ 780 nm	891	*Small*, 2025, 2409079
TD-COF@ZIS	H_2O, O_2	λ > 420 nm	3334	*J. Colloid Interface Sci.*, 2025, 694, 137670

COF-TPDB-NO_2	H_2O, Air	λ > 420 nm	1400	*Appl. Catal., B*, 2025, 371, 125263
TP/TAPT-F COF	H_2O, Air	λ > 420 nm	1655	*Chem. Eng. J.*, 2025, 515, 163722
20BTB	H_2O, O_2	λ > 420 nm	4088.46	*J. Colloid Interface Sci.*, 2025, 692, 137544
BBT-ACN COF-1	H_2O, Air	λ > 420 nm	2500	*Adv. Funct. Mater.*, 2025, 2424035–2424044
COF 4	H_2O/EtOH(9/1), O_2	λ > 420 nm	1839	*ACS Catal.*, 2025, 15, 10144–10153
TMB-COF-4	H_2O, O_2	λ > 420 nm	5106	*Angew. Chem. Int. Ed.*, 2025, 64, e202412890

Supporting References

1 M. J. Frisch, G. W. Trucks, H. B. Schlegel, G. E. Scuseria, M. A. Robb, J. R. Cheeseman, G. Scalmani, V. Barone, G. A. Petersson, H. Nakatsuji, X. Li, M. Caricato, A. V. Marenich, J. Bloino, B. G. Janesko, R. Gomperts, B. Mennucci, H. P. Hratchian, J. V. Ortiz, A. F. Izmaylov, J. L. Sonnenberg, Williams, F. Ding, F. Lipparini, F. Egidi, J. Goings, B. Peng, A. Petrone, T. Henderson, D. Ranasinghe, V. G. Zakrzewski, J. Gao, N. Rega, G. Zheng, W. Liang, M. Hada, M. Ehara, K. Toyota, R. Fukuda, J. Hasegawa, M. Ishida, T. Nakajima, Y. Honda, O. Kitao, H. Nakai, T. Vreven, K. Throssell, J. A. Montgomery Jr., J. E. Peralta, F. Ogliaro, M. J. Bearpark, J. J. Heyd, E. N. Brothers, K. N. Kudin, V. N. Staroverov, T. A. Keith, R. Kobayashi, J. Normand, K. Raghavachari, A. P. Rendell, J. C. Burant, S. S. Iyengar, J. Tomasi, M. Cossi, J. M. Millam, M. Klene, C. Adamo, R. Cammi, J. W. Ochterski, R. L. Martin, K. Morokuma, O. Farkas, J. B. Foresman, D. J. Fox, Wallingford, CT, 2016.

2 T. Lu, *J. Chem. Phys.*, 2024, **161**, 82503.

3 T. Lu and F. Chen, *J. Comput. Chem.*, 2012, **33**, 580–592.

4 W. Humphrey, A. Dalke and K. Schulten, *J. Mol. Graphics*, 1996, **14**, 33–38.

5 T. Lu and Q. Chen, *Comput. Theor. Chem.*, 2021, **1200**, 113249.

6 Q. Sun, B. Aguila, L. D. Earl, C. W. Abney, L. Wojtas, P. K. Thallapally and S. Ma, *Adv. Mater.*, 2018, **30**, 1705479.

7 L. Wang, L. Zhang, B. Lin, Y. Zheng, J. Chen, Y. Zheng, B. Gao, J. Long and Y. Chen, *Small*, 2021, **17**, 2101017.

8 P. Duan, D.-Y. Lin, W.-T. Yang, X.-J. Huang, A.-H. Sun and Q.-H. Pan, *Rare Met.*, 2022, **41**, 1323–1331.